DEVELOPMENT OF AN ACCURATE CENTRAL FINITE-DIFFERENCE SCHEME WITH A COMPACT STENCIL FOR THE SIMULATION OF UNSTEADY INCOMPRESSIBLE FLOWS ON STAGGERED ORTHOGONAL GRIDS

Elyas Larkermani*, Hans Bihs, Grégoire Winckelmans, Matthieu Duponcheel, Tobias Martin, Bernhard Müller, Laurent Georges*

Department of Energy and Process Engineering (EPT), Norwegian University of Science and Technology (NTNU), Gløshaugen campus, 7491 Trondheim, Norway

Department of Civil and Transport Engineering, Norwegian University of Science and Technology (NTNU), NO-7491 Trondheim, Norway

Université Catholique de Louvain (UCL), Institute of Mechanics, Materials, and Civil Engineering (iMMC), Louvain-La-Neuve, Belgium

Université catholique de Louvain (UCL), Mechanical Engineering Department, Division TERM, Center for Systems Engineering and Applied Mechanics (CESAME), 1348 Louvain-la-Neuve, Belgium

e-mail: elyas.larkermani@ntnu.no

ABSTRACT

In scale-resolving simulations such as Large Eddy Simulation (LES), the spatial discretization scheme of the convective term plays a crucial role to avoid the interference between the numerical errors and the subgrid-scale model. Accurate schemes lead to lower truncation errors, better predictions of turbulent flows, without the need for an excessively refined grid. To this end, a new second-order finite difference scheme (HCDS6) is developed for incompressible flows and orthogonal staggered grids. Compared to the standard second-order scheme of Harlow and Welch (CDS2), the new scheme has significantly lower dispersion errors. Compared to existing high-order schemes, the numerical stencil of HCDS6 is more compact, which makes it easier to implement, especially considering boundary conditions around complex geometries using immersed boundary methods (IBM). The HCDS6 scheme conserves the discrete momentum with limited production or dissipation of discrete kinetic energy, which guarantees its numerical stability. Its performance is evaluated using an open-source CFD package called REEF3D. Three benchmarks demonstrate the key properties and performance of the scheme: the convection of an isentropic vortex, the Taylor-Green vortex flow, and turbulent channel flow. Its relatively low dispersion errors combined with ease of implementation make the HCDS6 scheme a promising candidate for efficient scale-resolving simulations of turbulent flows.

Keywords:

INTRODUCTION

The purpose of this research is to construct accurate finite difference schemes for incompressible unsteady turbulent flow simulations such as Large Eddy Simulation (LES) or Direct Numerical Simulation (DNS). More specifically, the paper focuses on orthogonal non-uniform grids where complex geometries can be considered using immersed boundaries (IBM) [1]. In this context, different numerical methods can be applied so that the main framework used in the paper is first introduced.

Firstly, previous studies [2-7] have demonstrated the significant influence of numerical errors on the prediction accuracy of LES. Significant kinetic energy at high wavenumbers in LES requires a numerical scheme that performs well in this range. While spectral methods are known for their uniform accuracy at all wavenumbers, they do have inherent limitations concerning geometry and boundary conditions, making them less applicable in certain cases [8]. Furthermore, aliasing errors are important using spectral methods. These errors can lead to a degradation of the solution and negatively impact the accuracy of the simulation unless explicitly removed using filtering techniques [9]. Finite differences, finite volume and finite element methods have lower aliasing errors due to the damping at high wavenumbers [9]. They are often preferred in practical LES applications due to their computational efficiency and flexibility for boundary conditions [10]. For these numerical methods, the conservation of the discrete kinetic energy is an important property for the spatial discretization of the convective term of the momentum equation. Turbulence is characterized by a transfer of kinetic energy between the different turbulent flow scales. Therefore, the numerical scheme should not interfere in this process through artificial numerical dissipation. In explicit LES, the kinetic energy dissipation at the smaller flow scales should be left to the subgrid scale (SGS) model. Central schemes are known to be non-dissipative but, in general, they do not conserve the discrete kinetic energy. In practice, this may affect the numerical stability of under-resolved simulations, such as LES. Only a subset of central schemes has been tailored to enforce the discrete energy conservation (assuming negligible time integration errors) which guarantees numerical stability.

Secondly, collocated grids placing all the flow variables (i.e., the velocity and pressure fields) at the same points leads to the checkerboard problem. This effect can be avoided using stabilization or special interpolation techniques [11]. Although popular and widely used in LES, these techniques introduce some numerical dissipation [12]. Alternatively, the staggered grid arrangement does not suffer from the checkerboard problem (i.e., spurious pressure oscillations) by placing flow variables at different locations. This arrangement is difficult to apply for complex grids, like unstructured grids. However, the complexity is acceptable for orthogonal non-uniform grids, as discussed in the paper. Finally, it is also worth mentioning that Laizet and Lamballais [10] managed to introduce a high-order compact scheme for incompressible flow on orthogonal grids by using a semi-staggered arrangement (meaning that all the components of velocity are located at the same point but not pressure).

The remainder of the paper therefore discusses central finite differences on staggered orthogonal grids, with a special focus on the conservation of the discrete kinetic energy. Existing schemes in this category will be discussed which enables to introduce the originality of the new scheme proposed in the paper.

- One remarkable example is the second-order central finite differences scheme developed by Harlow and Welch for staggered meshes [13]. It proved to be well suited for DNS and LES of turbulent flow [14-17]. This scheme conserves not only the discrete mass and momentum but also the discrete kinetic energy on a non-uniform grid. The coefficients of the numerical stencil are not adapted as a function of the local grid stretching to conserve the skew-symmetry property of the discretization operator, and thus the discrete kinetic energy conservation. As coefficients are not adapted to the local grid stretching, Rivas [18] showed that this scheme has a first-order truncation error on a non-uniform grid but that it could achieve second-order accuracy on a continuously stretched grid. Although widely used for simplicity and efficiency, this second-order central scheme has large dispersion errors.

- Higher-order numerical schemes overcome the impact of truncation errors providing more accurate approximations and improving the fidelity of the resolved scales [19]. In addition to good resolution at high wavenumbers and low sensitivity to aliasing errors, the conservation properties of the high-order numerical scheme on staggered grids are a crucial aspect that contributes to high-fidelity LES [20]. Morinishi et al. [21] introduced high order finite differences (i.e., meaning fourth order and higher) on staggered orthogonal grids that conserve the discrete momentum and kinetic energy on uniform meshes. This scheme can be formulated in divergence, advective and skew-symmetric forms. Vasilyev [22] extended these schemes to non-uniform grids. The skew-symmetric form conserves the discrete energy but only conserves the discrete momentum on a uniform mesh while the divergence form conserves the discrete momentum but only conserves the discrete kinetic energy on a uniform mesh. In other words, none of the forms can simultaneously conserve the discrete momentum and kinetic energy on a non-uniform grid (called "commutation error" in Vasilyev et al. [22]). In parallel, Verstappen and Veldman [23, 24] introduced a fourth-order kinetic energy conserving finite volume method for orthogonal non-uniform meshes. The method is constructed based on the Richardson extrapolation of the classical second-order method. As the method is based on finite volumes, it is inherently in divergence form, but it preserves the skew-symmetry of the discretization operator. Unlike the finite difference of Vasilyev [22], the scheme of Verstappen et al. [24] can simultaneously conserve the discrete momentum and kinetic energy on a non-uniform mesh. For both schemes, the coefficients are not adapted locally as a function of the local grid stretching, like for the second-order scheme of Harlow and Welch [13]. Again, high-order accuracy is reached only if there is smooth mapping between the computational and physical spaces. The main challenge with these two schemes is that the numerical stencil is not compact, due to the use of high-order interpolations in the three spatial directions. These schemes are thus more complex to implement, and they make the treatment of boundary conditions complicated, especially for complex geometries in practical engineering problems using IBM.

Therefore, the paper introduces a new second-order numerical scheme with better numerical properties than the standard scheme of Harlow and Welsh on staggered grids. The scheme involves seven points in each spatial direction but remains compact, which simplifies the implementation and the treatment of boundary conditions. Although the scheme is formally second order, it is six-order accurate for linear advection problems, providing relatively low dispersion errors. Finally, the strict conservation of the discrete kinetic energy has to be sacrificed, but numerical tests introduced in the paper prove that it has a limited impact on results. The key properties of the new scheme are evaluated using three benchmarks: the convection of an isentropic vortex, three-dimensional Taylor-Green vortex flow, and the turbulent channel flow (in DNS and truncated Navier-Stokes simulation, TNS).

The paper is organized as follows. In Section 2, the discrete equations for the incompressible Navier-Stokes equations and the new scheme are introduced. Section 3 analyzed the performance of the new scheme on the three flow benchmarks. Section 4 concludes the paper by summarizing the findings and outlining future research directions.

Numerical method

- **Governing equations**

The incompressible Navier–Stokes equations are presented in Equation (1, which translates the mass and momentum conservation:

$$\frac{\partial u_m}{\partial x_m} = 0$$
$$\frac{\partial u_m}{\partial t} + \frac{\partial}{\partial x_j}(u_m u_n) = -\frac{1}{\rho}\frac{\partial p}{\partial x_m} + \frac{\partial}{\partial x_n}\left[\upsilon\left(\frac{\partial u_m}{\partial x_n} + \frac{\partial u_n}{\partial x_m}\right)\right] \tag{1}$$

Where x_m denotes the m^{th} spatial coordinate direction. u_m represents the velocity field in the x_m direction, t the time, p the pressure. The parameter υ is the kinematic viscosity.

Spatial discretization

A schematic of a bi-dimensional fully staggered grid arrangement where the velocity components are located at the cell surfaces while the pressure and other scalar quantities are stored in the cell center [11] is illustrated in Figure *1*. Here, i, j and k are mesh indices in the x_1, x_2 and x_3 directions, respectively.

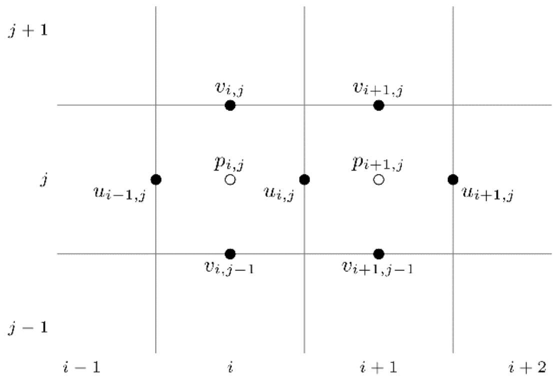

Figure 1. Staggered arrangement of variables in two dimensions.

Using the notation of Morinishi et al. [21], the finite difference $\left(\frac{\delta_n}{\delta_n x_1}\right)$ and the interpolation $(\bar{\phi}^{n x_1})$ operators in physical space with stencil n in direction x_1 acting on the field ϕ are respectively defined as:

$$\frac{\delta_n \phi}{\delta_n x_1}\Big|_{i,j,k} = \frac{\phi(x_1(i+n/2), x_2(j), x_3(k)) - \phi(x_1(i-n/2), x_2(j), x_3(k))}{x_1(i+n/2) - x_1(i-n/2)}$$
$$\bar{\phi}^{n x_1}\Big|_{i,j,k} = \frac{\phi(x_1(i+n/2), x_2(j), x_3(k)) + \phi(x_1(i-n/2), x_2(j), x_3(k))}{2} \tag{2}$$

These two operators can be directly extended to the other spatial directions. Using this notation, the standard second-order scheme of Harlow and Welsh (CDS2) for the non-linear convective term in Eq. **Error! Reference source not found.** can be written in the following way:

$$\frac{\delta(u_n u_m)}{\delta x_n}\Big|_{i,j,k} = \left[\frac{\delta_1}{\delta_1 x_n}\{\bar{u}_n^{1x_m}\,\bar{u}_m^{1x_n}\}\right]_{i,j,k} \tag{3}$$

For the new scheme (HCDS6), the convective term is also in divergence form but discretized using a symmetric, seven-point where the convection velocity is interpolated with the second-order accurate interpolation operator, whereas the convective fluxes are discretized using a high-order central interpolation scheme:

$$\frac{\delta(u_n u_m)}{\delta x_n}|_{i,j,k} = \left[\frac{\delta_1}{\delta_1 x_n}\{\bar{u}_n{}^{1x_m}\left(\alpha_1 \bar{u}_m{}^{1x_n} + \alpha_3 \bar{u}_m{}^{3x_n} + \alpha_5 \bar{u}_m{}^{5x_n}\right)\}\right]_{i,j,k} \tag{4}$$

with $\alpha_1 = 37/30$, $\alpha_3 = -8/30$ and $\alpha_5 = 1/30$ being the constant scheme coefficients, not adapted according to the local grid stretching. For $\alpha_1 = 1$, $\alpha_3 = 0$ and $\alpha_5 = 0$, the method is degraded to the standard second-order central differential scheme of Harlow and Welsch (CDS2). It can be observed that the new HCDS6 and CDS2 schemes are more compact than the fourth-order finite difference schemes of Vasilyev [22], for example, in divergence form (CDS4):

$$\begin{aligned}\frac{\delta(u_n u_m)}{\delta x_n}|_{i,j,k} = \Bigg[&\frac{9}{8}\frac{\delta_1}{\delta_1 x_n}\left\{\left(\frac{9}{8}\bar{u}_n{}^{1x_m} - \frac{1}{8}\bar{u}_n{}^{3x_m}\right)\bar{u}_m{}^{1x_n}\right\} \\ &-\frac{1}{8}\frac{\delta_1}{\delta_1 x_n}\left\{\left(\frac{9}{8}\bar{u}_n{}^{1x_m} - \frac{1}{8}\bar{u}_n{}^{3x_m}\right)\bar{u}_m{}^{3x_n}\right\}\Bigg]_{i,j,k}\end{aligned} \tag{5}$$

Using the definition of the finite difference and the interpolation operators in Equation (2) at the mesh indexes i, j and k, the new central scheme (HCDS6) for the convective terms in staggered grids can be rewritten. To simplify the notation, u_1 and u_2 are simplified to u and v and x_1 and x_2 to x and y, respectively:

$$\begin{aligned}
&\frac{\delta(uu)}{\delta x}|_{i,j,k} = \\
&= \frac{\frac{u_{i,j,k}+u_{i+1,j,k}}{2}\left(\alpha_1\frac{u_{i,j,k}+u_{i+1,j,k}}{2}+\alpha_3\frac{u_{i-1,j,k}+u_{i+2,j,k}}{2}+\alpha_5\frac{u_{i-2,j,k}+u_{i+3,j,k}}{2}\right)}{x_{i+1/2}-x_{i-1/2}} \\
&- \frac{\frac{u_{i-1,j,k}+u_{i,j,k}}{2}\left(\alpha_1\frac{u_{i-1,j,k}+u_{i,j,k}}{2}+\alpha_3\frac{u_{i-2,j,k}+u_{i+1,j,k}}{2}+\alpha_5\frac{u_{i-3,j,k}+u_{i+2,j,k}}{2}\right)}{x_{i+1/2}-x_{i-1/2}} \\
&\frac{\delta(uv)}{\delta y}|_{i,j,k} = \\
&= \frac{\frac{v_{i,j,k}+v_{i+1,j,k}}{2}\left(\alpha_1\frac{u_{i,j,k}+u_{i,j+1,k}}{2}+\alpha_3\frac{u_{i,j-1,k}+u_{i,j+2,k}}{2}+\alpha_5\frac{u_{i,j-2,k}+u_{i,j+3,k}}{2}\right)}{y_{j+1/2}-y_{j-1/2}} \\
&- \frac{\frac{v_{i,j-1,k}+v_{i+1,j-1,k}}{2}\left(\alpha_1\frac{u_{i,j-1,k}+u_{i,j,k}}{2}+\alpha_3\frac{u_{i,j-2,k}+u_{i,j+1,k}}{2}+\alpha_5\frac{u_{i,j-3,k}+u_{i,j+2,k}}{2}\right)}{y_{j+1/2}-y_{j-1/2}}
\end{aligned} \tag{6}$$

Compared to the CDS2, the HCDS6 does not significantly increase the computational time in the bulk of the computational domain. However, the situation is different near the boundaries as the numerical stencil of HCDS6 has seven points in each spatial direction. Firstly, it means that three layers of ghost points should be created for Dirichlet and Neumann boundary conditions. Secondly, in parallel computation, three layers of points should also be exchanged between partitions (considering a multiblock domain decomposition). This increases the amount of data to be exchanged between processors as the CDS2 only requires the communication of one layer of points.

- **Linear advection problem**

Consider the 1D linear advection equation of the form:

$$\frac{\partial u}{\partial t} + a\frac{\partial u}{\partial x} = 0 \quad (7)$$

where a is the constant advection velocity on the spatial domain $x \in [0,2\pi]$ with periodic boundary conditions. Using the new central difference scheme (HCDS6) defined in Equation (4 to discretize the convective term on a uniform mesh ($\Delta x = h$), the semi-discretized one-dimensional linear advection equation is obtained:

$$\frac{\partial u_i}{\partial t} + \frac{a}{2h}\left(\frac{1}{30}u_{i+3} - \frac{3}{10}u_{i+2} + \frac{3}{2}u_{i+1} - \frac{3}{2}u_{i-1} + \frac{3}{10}u_{i-2} - \frac{1}{30}u_{i-3}\right) = 0 \quad (8)$$

This spatial discretization is six order accurate, which explains why the new scheme has been given the acronym HCDS6. The modified wave number analysis can be performed. The details of the mathematical developments are given in Appendix. Figure *2*(a) shows that the non-dimensional modified wavenumber $k_{mod}h$ of the CDS2 and HCDS6 schemes almost follow the exact wavenumber up to about $\xi = kh = 0.4$ and 1.2, respectively. The non-dimensional modified wavenumber for CDS2 decreases from the maximum at $\xi = \pi/2$ to zero at $\xi = \pi$, while the $k_{mod}h$ for HCDS6 stays near the exact solution even at $\xi = \pi/2$, where $k_{mod}h = 1.47$.

Figure *2*(b) shows that the phase velocity for CDS2 and HCDS6 is close to the exact value a up to $\xi \approx 0.25$ and $\xi \approx 1.1$, respectively. Beyond $\xi \approx 0.25$ and $\xi \approx 1.1$, the waves computed with CDS2 and HCDS6 lag the exact waves, leading to large dispersion errors, especially for CDS2. At $\xi = \pi$, the computed waves are stationary.

The group velocity $(d\omega/dk)$ is the velocity at which groups of waves and also energy are transported. Figure *2*(c) indicates that HCDS6 computes the group velocity more correctly than CDS2. For $\xi \geq \pi/2$ groups of waves and energy are transported in the wrong direction with CDS2, while they are transported in the right direction with HCDS6. For $\xi = \pi$, $\frac{d\omega}{dk} = -a$ and $\frac{d\omega}{dk} = -2.2a$ for CDS2 and HCDS6, respectively. Remember that the exact group velocity is a.

Since HCDS6 better represents the phase velocity and group velocity at higher wavenumber than CDS2, we need fewer points per wavelength for HCDS6 than CDS2. In three dimensions, this can result in a significant reduction of the number of grid points to reach the same accuracy. It is worth noticing that, for a linear advection problem, the performance of HCDS6 is superior to the fourth-order accurate scheme of Vasilyev [22] (CDS4).

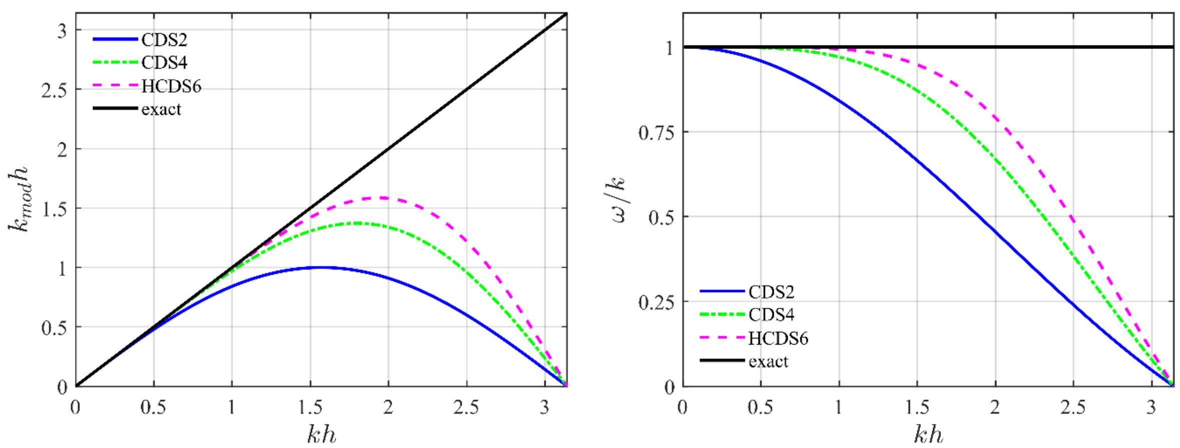

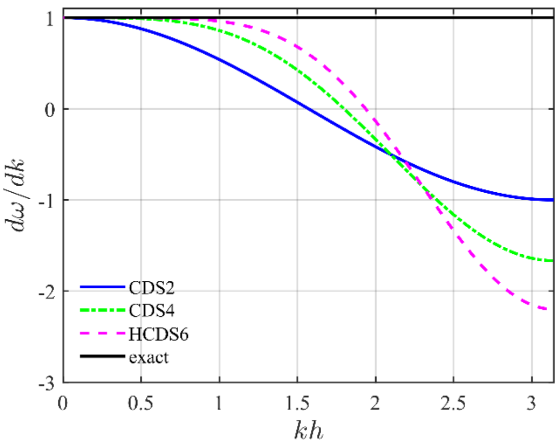

Figure 2 Non-dimensional modified wavenumber (a), phase velocity (b) and group velocity (c) for $a = 1$ with CDS2, CDS4 and HCDS6

Validation tests

In this section, three benchmark tests are carried out in the REEF3D flow solver [25] to demonstrate the properties and performance of the present numerical method, including the convection of an isentropic vortex, the three-dimensional Taylor-Green vortex flow, and turbulent channel flow simulations. REEF3D is an open-source CFD software package focusing on CFD in hydrodynamics, offshore, and environmental and marine engineering. It is a powerful high-order flow solver. REEF3D uses a ghost cell immersed boundary method to deal with complex geometry on an orthogonal grid [26]. The ghost cell method belongs to the general category of immersed boundary methods (IBM), which can potentially treat arbitrary immersed bodies on orthogonal meshes [27]. In REEF3D, incompressible Navier-Stokes equations are solved in parallel using domain decomposition. Partitions communicate with their neighbors using ghost cells and the Parallel Message Passing Interface (Parallel MPI) [25]. The current simulations were performed on the FRAM machine provided by UNINETT Sigma2, the National Infrastructure for High-Performance Computing and Data Storage in Norway. The Linux cluster FRAM is a distributed memory system that consists of 1004 dual socket and two quad socket nodes, interconnected with a high-bandwidth, low-latency Infiniband network. The interconnect network is organized in an island topology, with 9216 cores in each island. Each standard compute node has two 16-core Intel Broadwell chips (2.1 GHz) and 64 GiB memory. In addition, eight larger memory nodes with 512 GiB RAM are available, catering to computational tasks that demand substantial memory resources for more complex simulations and data-intensive processing. The total number of compute cores is 32256.

In REEF3D, the pressure velocity coupling is done using the projection method proposed by Chorin [28]. Then, the computation of velocity and pressure is decoupled and performed in three steps. During the first step, the method proceeds by neglecting the incompressibility constraint to compute an intermediate velocity field u^* using equation (9):

$$\frac{u_m^* - u_m^k}{\Delta t} + \frac{\delta}{\delta x_n}(u_n^k u_m^k) = -\frac{1}{\rho}\frac{\delta p^k}{\delta x_m} + \frac{\delta}{\delta x_n}\left[\upsilon\left(\frac{\delta u_m^k}{\delta x_n} + \frac{\delta u_n^k}{\delta x_m}\right)\right] \tag{9}$$

where u_m^k is the velocity at k^{th} time step. Note that the resulting intermediate velocity u_m^* does not satisfy the continuity equation (Eq. (1)

). To enforce continuity, the intermediate velocity is projected onto the space of incompressible divergence-free vector fields to obtain u_m^{k+1}:

$$\frac{u_m^{k+1} - u_m^*}{\Delta t} = -\frac{1}{\rho}\frac{\delta_1 (p^{k+1} - p^k)}{\delta_1 x_m} \tag{10}$$

This is done by solving a Poisson equation for the pressure field using the divergence of the intermediate velocity field and enforcing $\frac{\delta_1 u_m^{k+1}}{\delta_1 x_m} = 0$. The fully parallelized Jacobi-preconditioned Bi-Conjugate Gradients Stabilized (BiCGStab) algorithm [29] solves the resulting Poisson pressure equation using geometric multigrid preconditioning provided by the high-performance solver library, HYPRE [30].

$$\frac{\delta_1}{\delta_1 x_m}\left(\frac{1}{\rho}\frac{\delta_1 (p^{k+1} - p^k)}{\delta_1 x_m}\right) = -\frac{1}{\Delta t}\frac{\delta_1 u_m^*}{\delta_1 x_m} \tag{11}$$

The result is a pressure field that enforces the incompressibility constraint on the velocity field. Finally, the new velocity field u_m^{k+1} at time step $k+1$ is obtained by subtracting the gradient of the pressure field from intermediate velocity (Eq. (10)). This results in a velocity field that satisfies both the momentum equation and the continuity equation.

By default, the governing equations are advanced in time using a fully explicit third-order Total Variation Diminishing (TVD) Runge-Kutta scheme [31]. At each Runge–Kutta substep, the project method of Chorin is applied so that all the substep velocity fields are divergence-free and the Poisson equation is solved three times per time step [32].

For the viscous terms and the pressure term, the second-order central differential scheme is adopted:

$$\frac{\delta}{\delta x_n}\left[\frac{\delta u_m}{\delta x_n}\right]|_{i,j,k} = \frac{\delta_1}{\delta_1 x_n}\left\{\frac{\delta_1 u_m}{\delta_1 x_n}\right\}|_{i,j,k} \tag{12}$$

- Convection of an Isentropic Vortex

In order to test the performance of the HCDS6 scheme concerning its dissipation and dispersion properties, the convection of a bi-dimensional isentropic vortex is considered. The vortex is convected by a uniform flow in the positive x direction. The initial solution is represented by the velocity components in the x and y directions.

$$\binom{u}{v} = \binom{u_\infty}{0} + u_A e^{(1-(r/b)^2)/2}\begin{pmatrix}(y-y_0)/b \\ -(x-x_0)/b\end{pmatrix} \tag{13}$$

with $r^2 = (x-x_0)^2 + (y-y_0)^2$ is the distance from the vortex center (x_0, y_0). The circumferential velocity induced by the vortex reaches its maximum value (u_A) at $r = b$. The vortex is translated with a mean-flow velocity in the x-direction within a bidimensional periodic domain. To minimize the impact of the boundary conditions and geometry on the results, a large computational domain with a dimension of $x \in [-25L, 25L]^2$ is considered. Here $L = \sqrt{\ln 2}b$ is a representative length scale of the vortex where $e^{-(r/b)^2} = 1/2$ at $r = L$.

A strong vortex with $u_A/u_\infty = 0.8$ is convected from the initial location at $(x_0, y_0) = (-18.75L, 0)$ to the final position $(x, y) = (18.75L, 0)$ for a time period of $u_\infty t/L = 37.5$ on a uniform Cartesian grid.

- Verification and Consistency

The root-mean-square (RMS) error between the numerical and analytical solutions as a function of the grid resolution for the CDS2 and HCDS6 schemes is shown in Figure *3*.

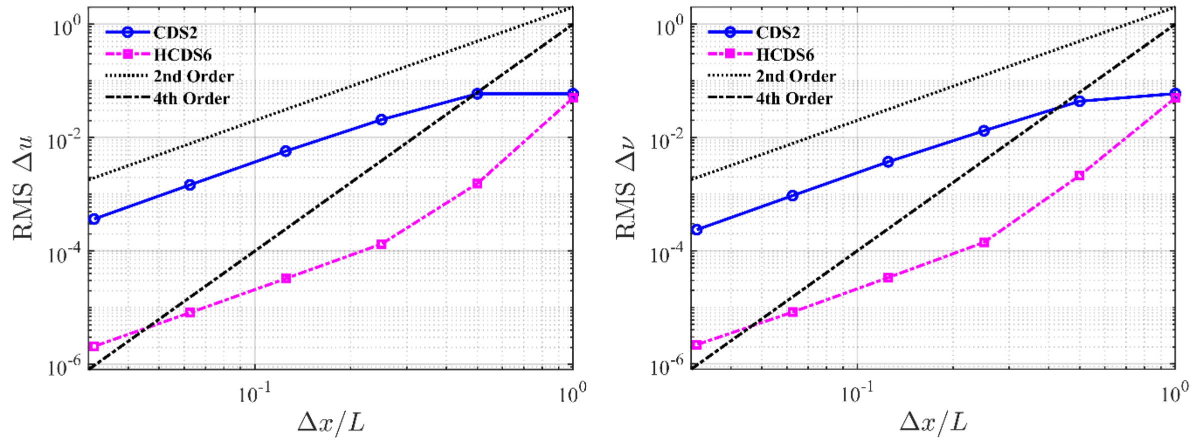

Figure 3 Convection of strong isentropic vortex on a uniform grid: grid dependence of the root-mean-square value of difference with the analytical solution at the time $u_\infty t/L = 37.5$. Left: velocity component u, right: velocity component v

Figure *3* shows that the HCDS6 scheme is indeed second-order accurate, while the fourth-order convergence is achieved on a uniform mesh for the second and third refinement steps. For smaller cell sizes than $L/4$, the discretization error of second-order starts to dominate the global error. However, the error is reduced by approximately two orders of magnitude for the HCDS6 compared to the standard CDS2. On the coarsest grid with $\Delta x = L$, CDS2 scheme turned out to be unstable.

- Shape and position of the vortex

The local resolution of the vortex on two different grid sizes ($\Delta x = L/2, L/4$) is shown in Figure *4*. Here, the y velocity component along the midline at $y = 0$ are compared with the analytical solution. For CDS2, the vortex has clearly lost its shape on a coarse grid ($\Delta x = L/2$), while it is better preserved by the lower dispersion error of the HCDS6. A close agreement to the analytical curve is achieved. As the mesh is further refined, the vortex shape is improved significantly by the CDS2 scheme, while the improvement for HCDS6 is minor as the solution was already accurate on the coarser mesh. The vortex center is drifted upward using the CDS2 scheme due to the dispersion error, indicated by a smaller difference between the numerical and analytical solution for the positive peak than the negative one. In other words, the vortex consists of a collection of waves with different wavelengths that are propagated at different velocities. Using the CDS2 scheme, the waves with low wave numbers are propagated at the correct speed, while the ones with higher wave numbers are traveling at the wrong speed. Consequently, those not propagated correctly are lagging and oscillating as a result of the dispersion error. In addition, the amplitude of low wave numbers is carried correctly. In contrast, the amplitude carried by the higher wave numbers appears as oscillation and reduces the vortex peak amplitude. The HCDS6 outperforms the CDS2 in maintaining the shape and position of the vortex.

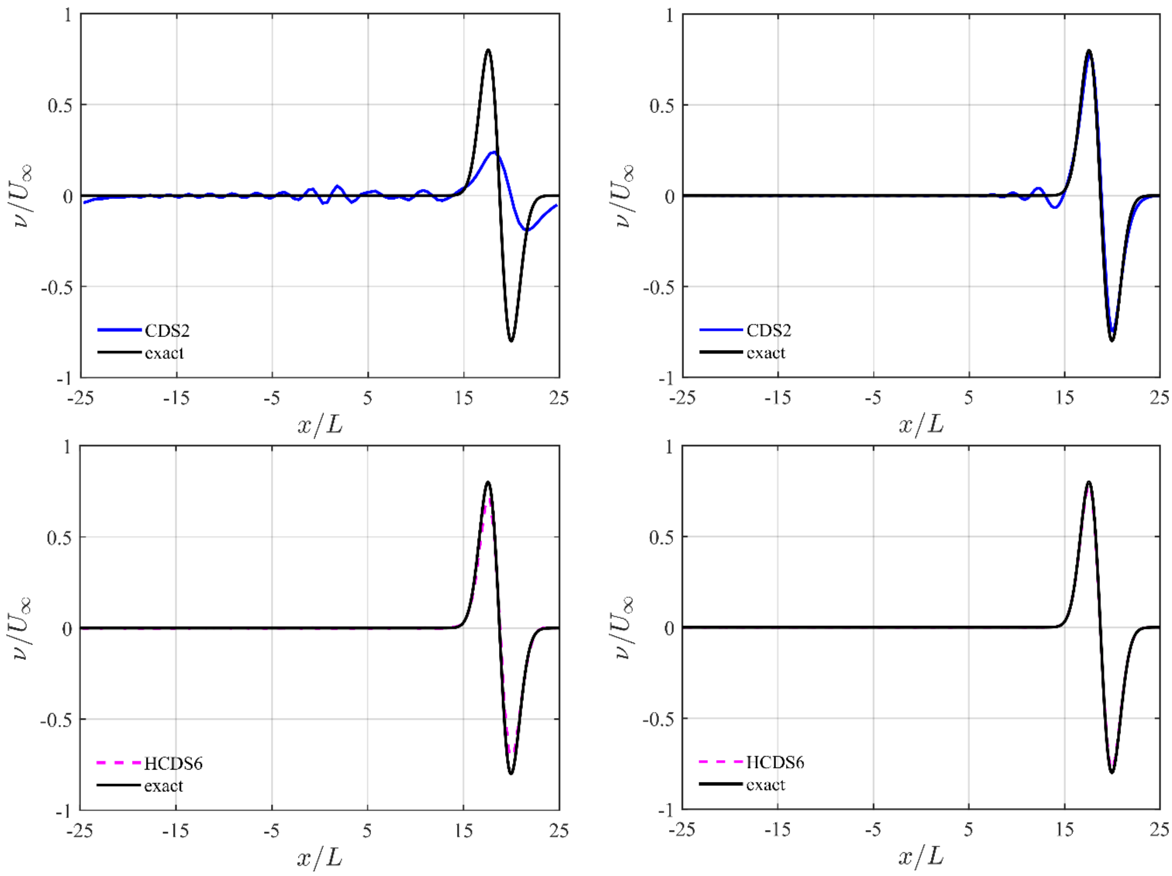

Figure 4 y velocity component along the midline at $y = 0$. Left: coarse grid ($\Delta x = L/2$), right: fine grid ($\Delta x = L/4$)

- 3D Taylor-Green vortex flow

The 3D Taylor-Green vortex flow is a well-defined, time-dependent, three-dimensional flow that is generated by the interaction of two counter-rotating vortices in a periodic cubic domain. This classic benchmark problem is typically used to validate numerical methods for scale-resolving simulations [33]. Interactions between different scales of motion in the fluid, driven by the nonlinear advection term in the Navier-Stokes equations, lead to the formation of smaller-scale vortices through vortex stretching, filamentation, and reconnection. These features are responsible for transferring energy from large-scale motion to smaller scales through the energy cascade.

The counter-rotating vortices are initialized in a checkerboard arrangement from an analytical periodic vortex field where a sinusoidal velocity field with a uniform vorticity distribution in the x-y plane is specified:

$$\begin{gathered}\frac{u}{U} = sin\left(\frac{x}{L}\right) cos\left(\frac{y}{L}\right) cos\left(\frac{z}{L}\right)\\ \frac{v}{U} = -cos\left(\frac{x}{L}\right) sin\left(\frac{y}{L}\right) cos\left(\frac{z}{L}\right)\\ \frac{w}{U} = 0\end{gathered} \tag{14}$$

Where L and U are the characteristic length and velocity scales of the problem, respectively. The Reynolds number of the flow is defined as $Re = \frac{UL}{\upsilon}$ and is equal to 1600. A periodic cubic domain with a periodicity length of $\mathcal{L}_x = \mathcal{L}_y = \mathcal{L}_z = 2\pi L$ is considered. A uniform grid is adopted with a same resolution in all three directions as $h = 2\pi L/N$ where N is the number of grid cells in one direction. The characteristic convective time $t_c = L/U$ is defined as the time required for a fluid particle to traverse the characteristic length scale of the flow (L) at the characteristic velocity scale (U). A non-dimensional physical time step of $\Delta t^* = \Delta t/t_c = 0.001$ is adopted to capture the temporal scales adequately. The physical time step size is halved for each subsequent grid refinement. The simulations are performed for a time period of $t/t_c = 10$.

Different diagnostics are introduced to evaluate the performance of the HDCS6 for Taylor-Green vortex flow simulation. A common diagnostic is the temporal evolution of the kinetic energy averaged over the control volume (V):

$$E_k = \frac{1}{V}\int_V \frac{u_i u_i}{2} dV \tag{15}$$

As the kinetic energy is not expected to vary much between the different scenarios investigated here , the time derivative of the total kinetic energy, defined as kinetic energy dissipation (ϵ), is a more sensitive characteristic than the total kinetic energy:

$$\epsilon = -\frac{dE_k}{dt} \tag{16}$$

- Verification and Consistency

The evolution of the global kinetic energy is plotted in Figure *5* for two different grid sizes with 256^3 and 512^3 cells, respectively. It is compared with the reference solution from a direct numerical simulation (DNS) computed using a pseudo-spectral code. Even at the coarsest resolution, both CDS2 and HCDS6 are in good agreement with pseudo-spectral. Hence, the temporal evolution of the kinetic energy is not sensitive to discriminate between the performance of the two central schemes. Therefore, the temporal development of the total kinetic energy dissipation rate is considered.

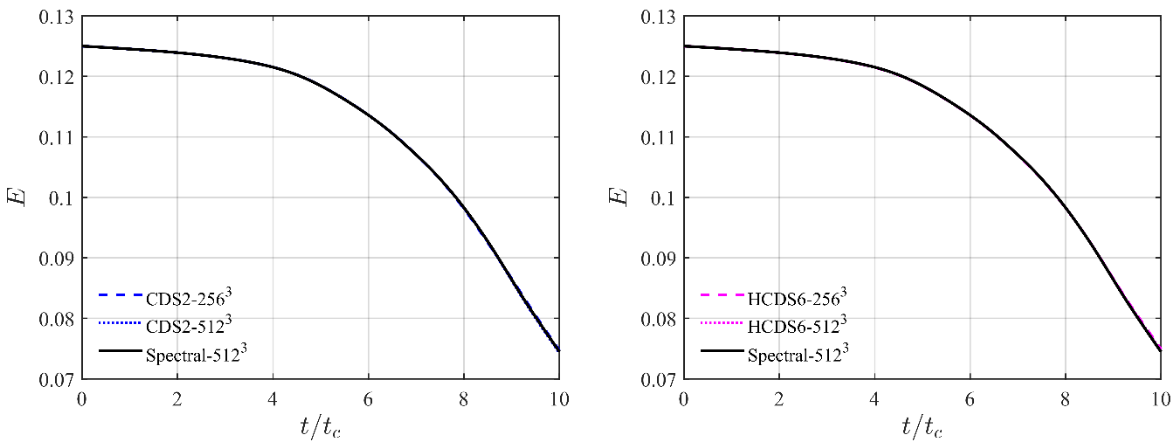

Figure 5 Temporal evolution of the global kinetic energy

- Evolution of the dissipation based on the time derivative of the total kinetic energy

Figure *6* depicts the evolution of the kinetic energy-based dissipation rate using two grid resolutions compared to the reference DNS solution. It is characterized by an initial rapid increase in dissipation rate associated with the formation and stretching of the initial vortices, followed by a gradual decay to a steady-state value for $t/t_c \geq 20$. As these vortices interact and break down, they transfer energy to smaller scales, increasing the dissipation rate. However, as the flow evolves and the vortices continue to break down, the dissipation rate eventually reaches a steady-state value, indicating that the energy injection and dissipation are balanced.

To assess the performance of the numerical scheme, a comparison between second-order CDS2 and HCDS6 on a low-resolution grid (256^3) is carried out. At around $t/t_c \approx 4$, the dissipation rate increases rapidly when the transition from simple initial vortices to small-scale anisotropic turbulence occurs. This increase reaches the dissipation peak at around $t/t_c \approx 9$. For the highest under-resolution computation with 256^3 grid cells, the HCDS6 scheme deviates from the pseudo-spectral results around $t/t_c \approx 8.6$ and underpredicts the dissipation peak up to $t/t_c = 10$. As the grid is refined, the numerical dissipation rate converges to the reference solution.

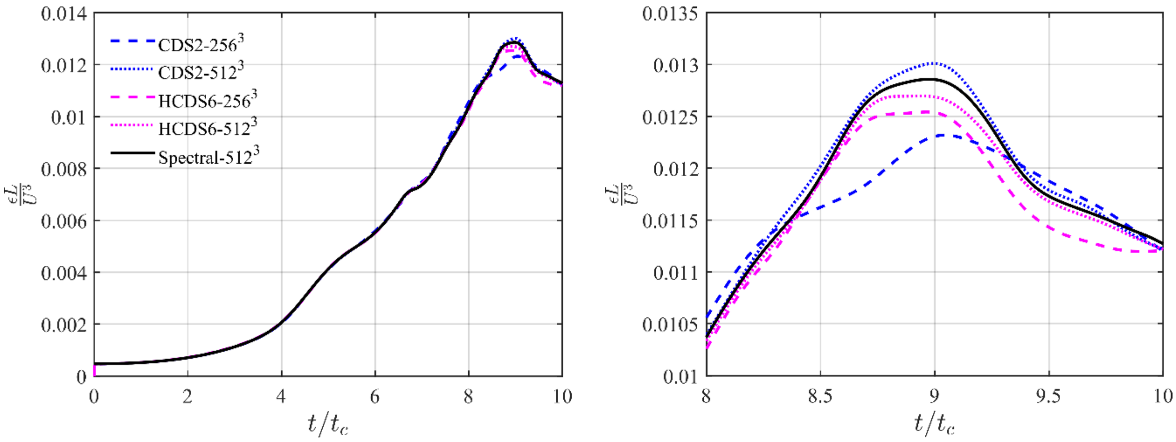

Figure 6 Temporal evolution of the dissipation rate based on kinetic energy

- Vortical structures

Regular counter-rotating vortices stretch and twist as the flow evolves, generating smaller and more complex vortical structures. These structures continue to interact with each other, leading to the formation of the most intricate vortices close to the dissipation peak at $t/t_c \approx 9$. Hence, a comparison of the instantaneous vorticity field is performed to analyze the accuracy and reliability of the numerical scheme to transport complex vortical structures. It is sufficient to visualize vortical structures only on a limited portion $(1/16)$ of the periodic plane, as the remaining portions will be identical due to different symmetries of the flow illustrated in Figure *7*.

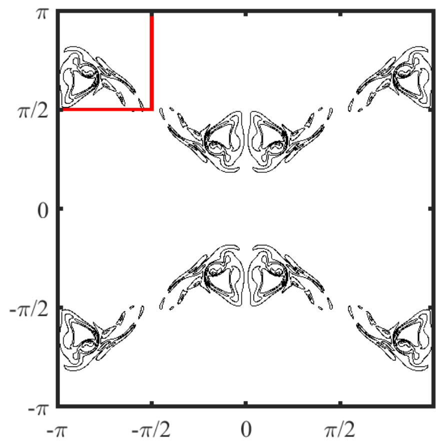

Figure 7 Instantaneous vorticity norm from the pseudo-spectral scheme on the periodic plane $(y = 0)$ at $t/t_c = 9$.

The vorticity isocontours for $\omega \in [1,5,10,20,30]$ on a subset of the periodic plane $(y = 0)$ at $t/t_c = 9$ obtained by CDS2, CDS4 and HCDS6 schemes are superposed with those from the pseudo-spectral scheme as a reference solution. The results are presented for two different grid resolutions of 256^3 and 512^3 in the left and right columns, respectively. On the coarse grid, the position of the large vortical structures is somewhat captured by the CDS2 and CDS4 schemes, while the smaller vortices are diffused and contaminated by numerical noise. The HCDS6 scheme can capture the vortical structures better, although small details of the solution are smeared. The shape of the vortex structure improves and overlaps with the reference spectral solution as the grid is refined using all three schemes.

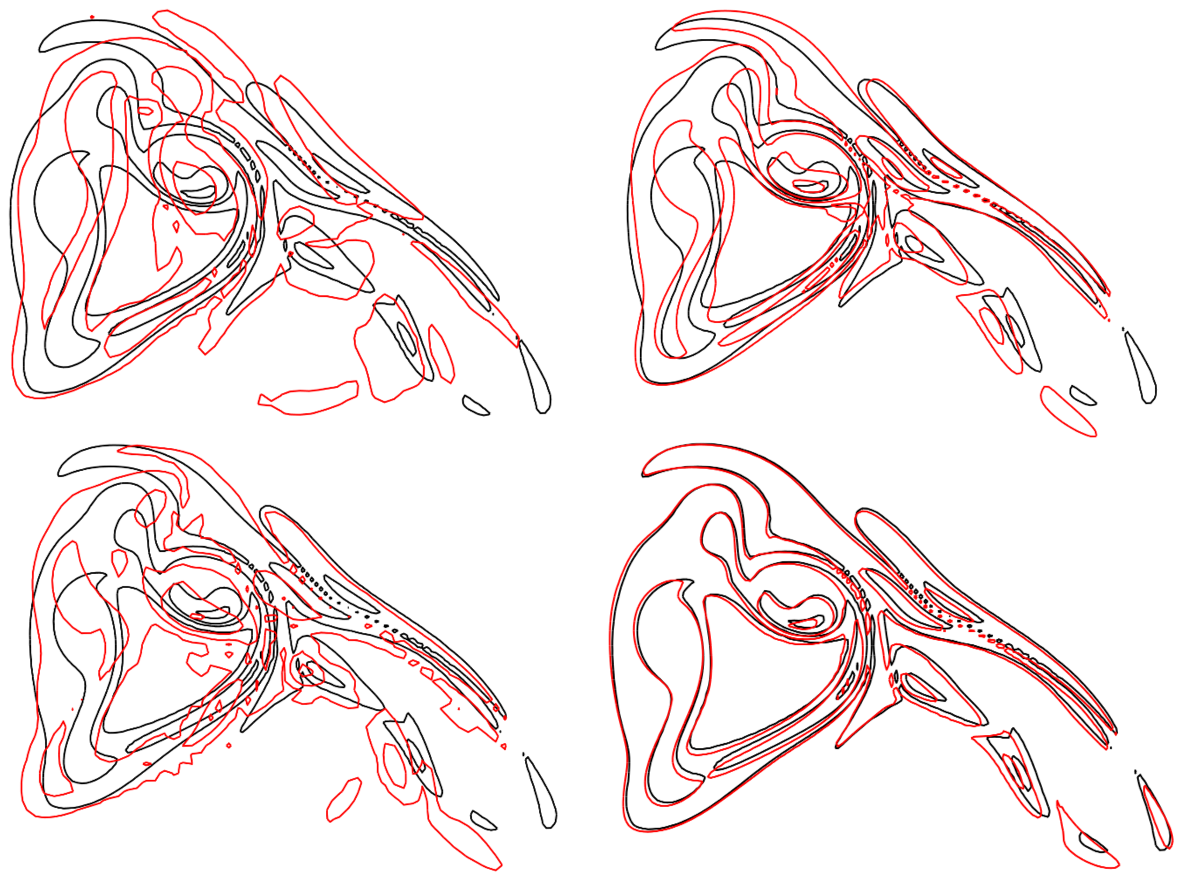

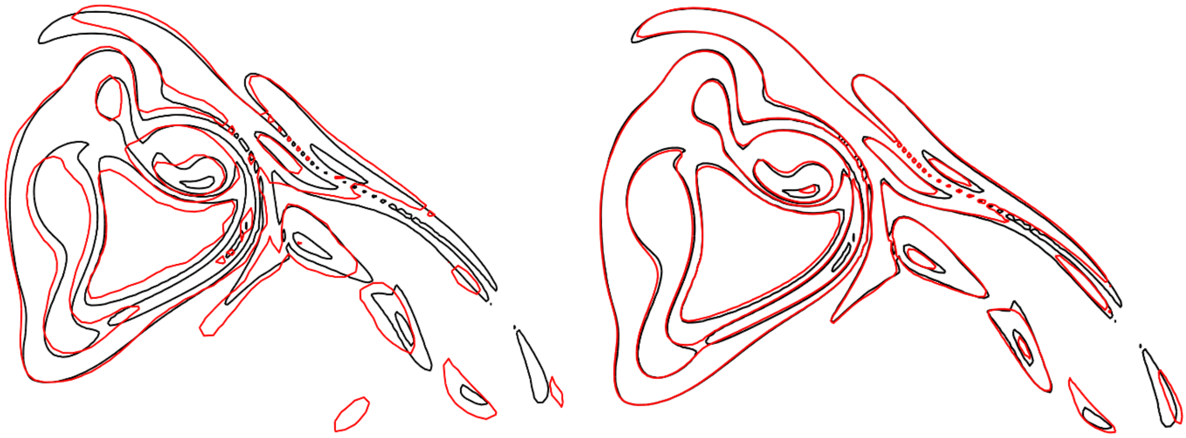

Figure 8 Iso-contours of the vorticity norm on the periodic plane ($y = 0$) at $t/t_c = 9$. Spectral slution in black and FD in red. Left: coarse grid (256^3), right: fine grid (512^3). Top: CDS2, middle: CDS4 bottom: HCDS6.

- Computation of Turbulent Channel Flows

Numerical simulations of turbulent channel flow are performed to assess the performance of the new HCDS6 scheme. It is an insightful flow benchmark. Firstly, the flow is bounded with a no-slip boundary condition, which generates turbulence. Secondly, previous test cases were performed on a uniform mesh while a grid stretching was applied in the wall-normal direction for the channel flow. Finally, the under-resolved channel flow is very sensitive to spurious production and dissipation of the discrete kinetic energy. Uncontrolled numerical dissipation strongly impacts the flow statistics, while significant spurious discrete kinetic energy production can lead to numerical instability.

In this benchmark, a fully developed turbulent flow is created between two infinite parallel plates separated by a distance 2δ. A constant adverse pressure gradient is applied to the flow in the streamwise direction to drive the flow through the channel. The no-slip condition is set for the top and bottom walls. Periodic boundary conditions are applied in the streamwise and spanwise directions to approximate infinite homogenous directions. These periodic boundaries should be placed far enough from each other that the largest vortical structures would not intersect the computational domain. A uniform grid is adopted in the periodic directions while the grid is stretched in the direction normal to the wall to resolve the boundary layers properly. This grid stretching is based on a hyperbolic tangent function:

$$x_j = -\frac{tanh\left(\gamma\left(1-\frac{2j}{N}\right)\right)}{tanh\,\gamma} \qquad j = 0,1,\dots,N \tag{17}$$

Here, N is the number of grid points in the j direction, and γ is the stretching factor.

A significantly small time step is selected to capture temporal scales precisely and keep the Courant number below one, guaranteeing numerical stability.

- Verification and Consistency

In this section, the DNS of turbulent channel flow at the frictional Reynolds number of $Re_\tau = 180$ is carried out to verify the consistency of the HCDS6, meaning whether the results converge to the correct solution as the grid resolution is refined. These results are compared to DNS data obtained using a spectral code [34, 35].

A same computational domain as Moser et al. of $L_x = 4\pi\delta,\ L_y = 2\delta,\ L_z = 4\pi/3\delta$ is used. The grid resolution is $N_x = 256,\ N_y = 256,\ N_z = 256$ where N_x, N_y and N_z are the number of cells in x, y and z directions, respectively. The stretching factor taken is equal to 1.6. The corresponding non-dimensional grid spacings in wall units are reported in Table *1*.

Table 1 Channel flow mesh resolution

Re_τ	Δx^+	Δz^+	Δy^+
180	8.836	2.945	$\in [0.372 - 2.441]$

The computational domain is initialized with a random solenoidal velocity field. For this specific test case, the default explicit time integration scheme is not used. A semi-implicit time marching algorithm is rather applied with the implicit Crank Nicholson for the diffusion term and an explicit third-order Runge-Kutta method for the other terms. The bulk time scale $(t^* = L_x/U_b)$ is equivalent to a flow-through time (FTT) of the domain, which corresponds to how long it takes for the fluid to traverse the entire computational domain at a constant mean bulk velocity (U_b). Once the flow has reached a statistical steady state, the flow statistics are averaged in the streamwise and spanwise homogeneous directions over a time interval of $50\delta/u_\tau$ approximately equivalent to 37 flow-through times, ensuring fully converged statistics.

The mean streamwise velocity profile (U^+), the total Reynolds shear stress $\left(T_{xy}\right)$ and square root of the second-order velocity moments normalized by the friction velocity are shown in Figure *9* as a function of the dimensionless distance to the wall.

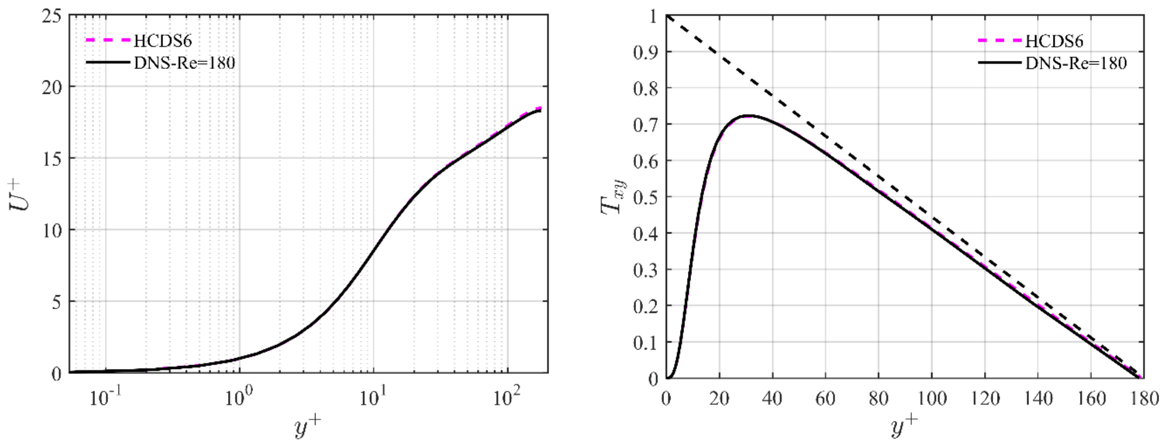

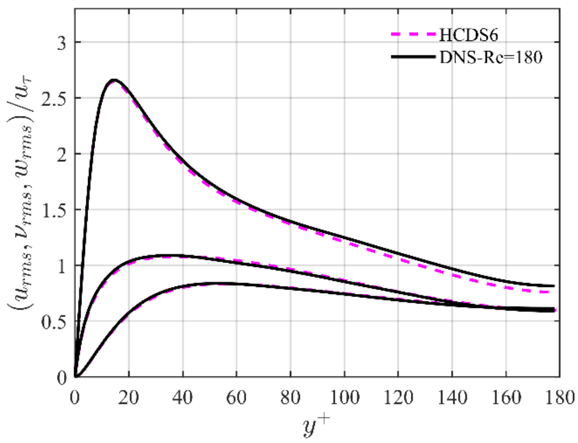

Figure 9 Total Reynolds shear stress (top left), mean streamwise velocity normalized by the DNS shear velocity (top right), square root of the second order velocity moments (bottom) for the DNS of turbulent channel flow at $Re_\tau = 180$.

The HCDS6 solution is in excellent agreement with the reference DNS results. The mean total Reynolds shear stress compares relatively well with the DNS data shown in the top left graph of Figure *9*. Investigating turbulence intensities involves analyzing the individual components of the total stress tensor illustrated at the bottom of Figure *9*. The predictions for the spanwise (w_{rms}) and wall-normal (v_{rms}) turbulence intensity components overlap with the DNS reference of Moser et al. The streamwise component (u_{rms}) exhibit only a slight deviation for y^+ above 80. All the predictions confirm the consistency of the HCDS6 scheme on non-uniform meshes.

- TNS of the channel flow at $Re_\tau = 180, 640, 950$

In contrast to DNS which resolves all the turbulent scales, the solver performance in marginally resolved simulations termed truncated Navier-Stokes simulations (TNS) is also investigated. In TNS, no turbulence modeling is applied. The same setup as DNS of turbulent channel flow is carried out at three frictional Reynolds numbers of $Re_\tau = 180, 640\ and\ 950$ but on a coarser mesh. In addition, the grid stretching is increased compared to the DNS and is made representative of LES applications. The computational domain size, grid resolution and corresponding non-dimensional grid spacings for each frictional Reynolds number are provided in Table *2*.

Table 2 Computational domain size and mesh densities for TNS of channel flow at$Re_\tau = 180, 640, 950$

Re_τ	L_x	L_y	L_z	N_x	N_y	N_z	Δx^+	Δz^+	Δy^+	γ	FTT
180	$2\pi\delta$	2δ	$\pi\delta$	128	128	128	8.96	4.48	$\in [0.12 - 14.4]$	2.8	42
640	$2\pi\delta$	2δ	$\pi\delta$	128	128	128	31.6	15.8	$\in [0.43 - 29.7]$	2.8	175
950	$2\pi\delta$	2δ	$\pi\delta$	128	128	128	45.7	22.9	$\in [0.63 - 37.1]$	2.8	266

- Mean streamwise velocity profile

The mean normalized streamwise velocity profiles for three frictional Reynolds numbers of $Re_\tau = 180, 640, 950$ along the channel height are shown in Figure *10*. The two discretization schemes agree well with the DNS data at $Re_\tau = 180$. For higher frictional Reynolds numbers, HCDS6 and DNS profiles almost collapse within the viscous sub-layer and buffer layer with a slight underprediction in the logarithmic inertial layer. However, the buffer layer, log layer and the outer region are strongly affected using the CDS2 scheme, where it starts to deviate from the reference in the buffer layer at $y^+ \approx 10$..

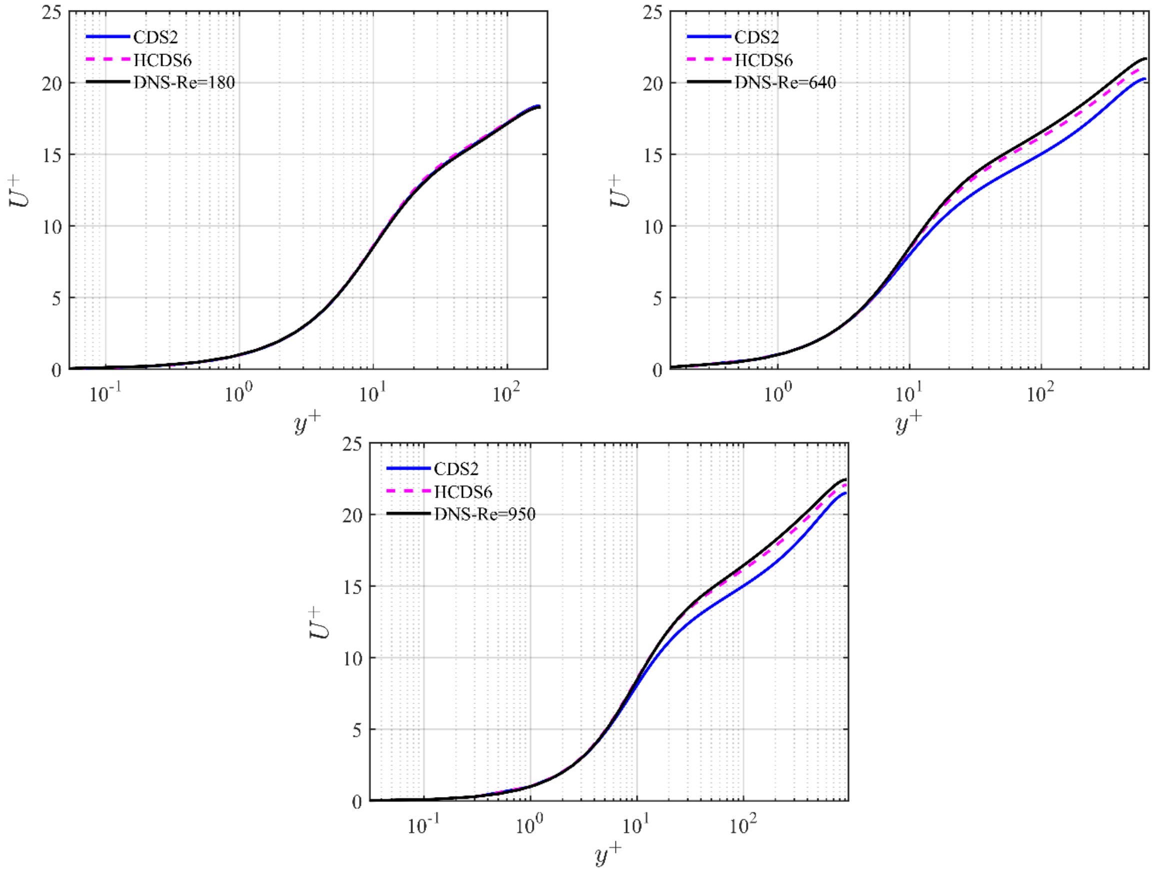

Figure 10 Mean streamwise velocity normalized by the DNS shear velocity for the TNS of turbulent channel flow at $Re_\tau = 180, 640, 950$.

- Total Reynolds shear stress

The non-dimensional profiles of mean total Reynolds shear stress at three frictional Reynolds numbers is depicted as a function of the distance from the wall to the center of the channel in Figure *11*. In a fully developed channel flow, the shear stresses and velocity gradients are more significant near the wall, indicated by a peak that decreases gradually to the channel centerline as the interaction between the mean velocity profile and the turbulent fluctuations is dampened. For all three frictional Reynolds numbers, CDS2 and HCDS6 can properly reproduce the total Reynolds shear stress of DNS. As the Reynolds number increases in a fully developed channel flow, the peak values of non-dimensional Reynolds stress near the channel walls become more pronounced due to higher turbulence intensity. Moreover, stronger velocity gradients near the walls contribute to a steeper slope of the Reynolds stress profile in this region and promote more efficient mixing and transport of momentum across the flow cross-section. With higher Reynolds numbers, the peak location is shifted toward the wall due to the altered balance between turbulent production and dissipation.

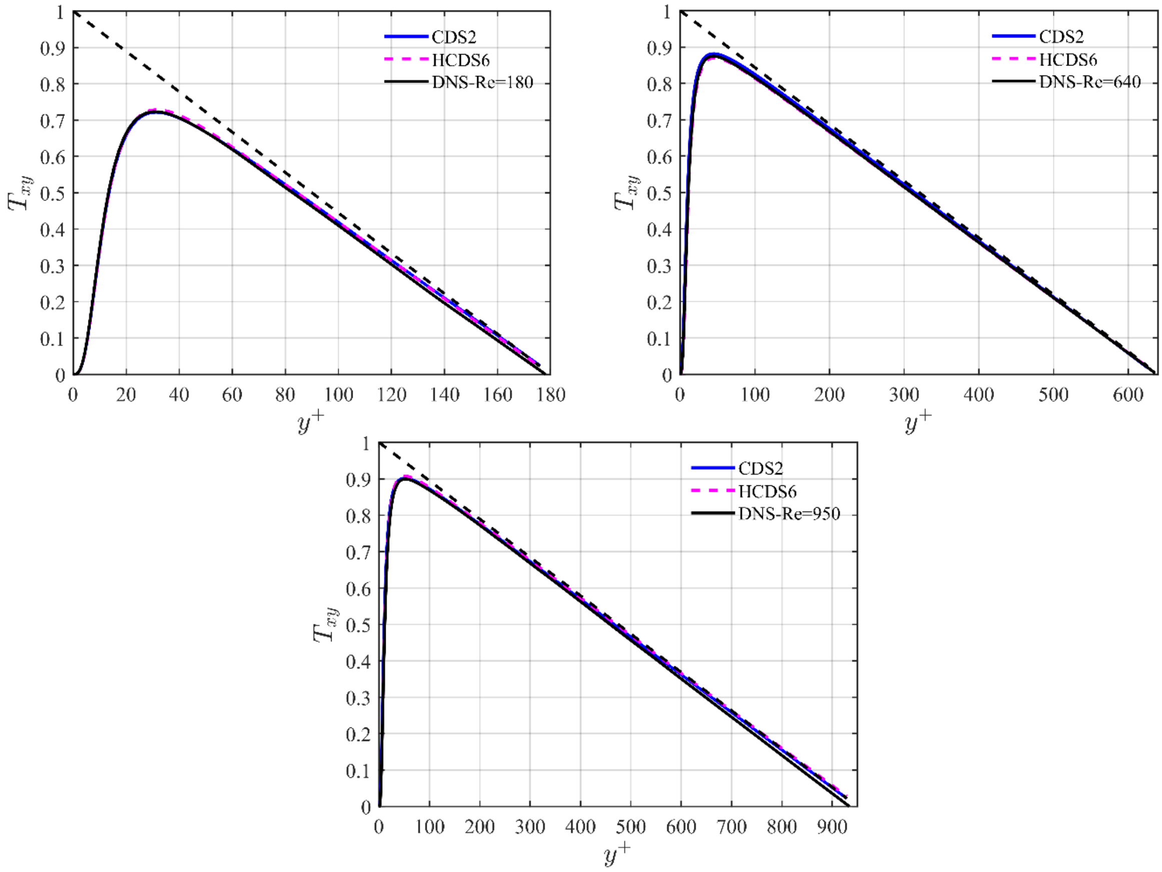

Figure 11 Total Reynolds shear stress for the TNS of turbulent channel flow at $Re_\tau = 180, 640, 950$.

- Velocity fluctuations

A comparison of mean normalized velocity fluctuations to DNS data is plotted in Figure *12*. For turbulent channel flow at a low Reynolds number of $Re_\tau = 180$, CDS2 perform an excellent job of representing all three components of the total stress tensor in the near wall and core section of the flow. However, the results from HCDS6 predict a slight overprediction, particularly for u_{rms} shear stress distribution when y^+ exceeds 10. By increasing the frictional Reynolds number to $Re_\tau = 640$, all the predictions of HCDS6 for the three velocity fluctuations remain accurate across the channel height, while significant deviations from the DNS data are observed for the CDS2 with reduced values of u_{rms} in buffer and log layer. Both the spanwise and wall-normal components, w_{rms} and v_{rms}, are underpredicted with the CDS2 scheme for the buffer layer and outer region in the core of the flow. The agreement of turbulent intensity components with DNS at a higher Reynolds number of $Re_\tau = 950$ clearly shows the superiority of the HCDS6 scheme compared to the CDS2. The exception being streamwise stresses, u_{rms}, that fails to capture the peak intensity in the vicinity of the wall. The deviation is more pronounced for CDS2, where the elevated prediction of the peak is followed by an underprediction away from the wall. Similar to $Re_\tau = 640$, wall-normal velocity fluctuation shows an underprediction for wall units of approximately 20 up to 210, and it is more pronounced in the outer region for y^+ above 800. Again HCDS6 successfully reproduces the DNS profile of w_{rms} and v_{rms}.

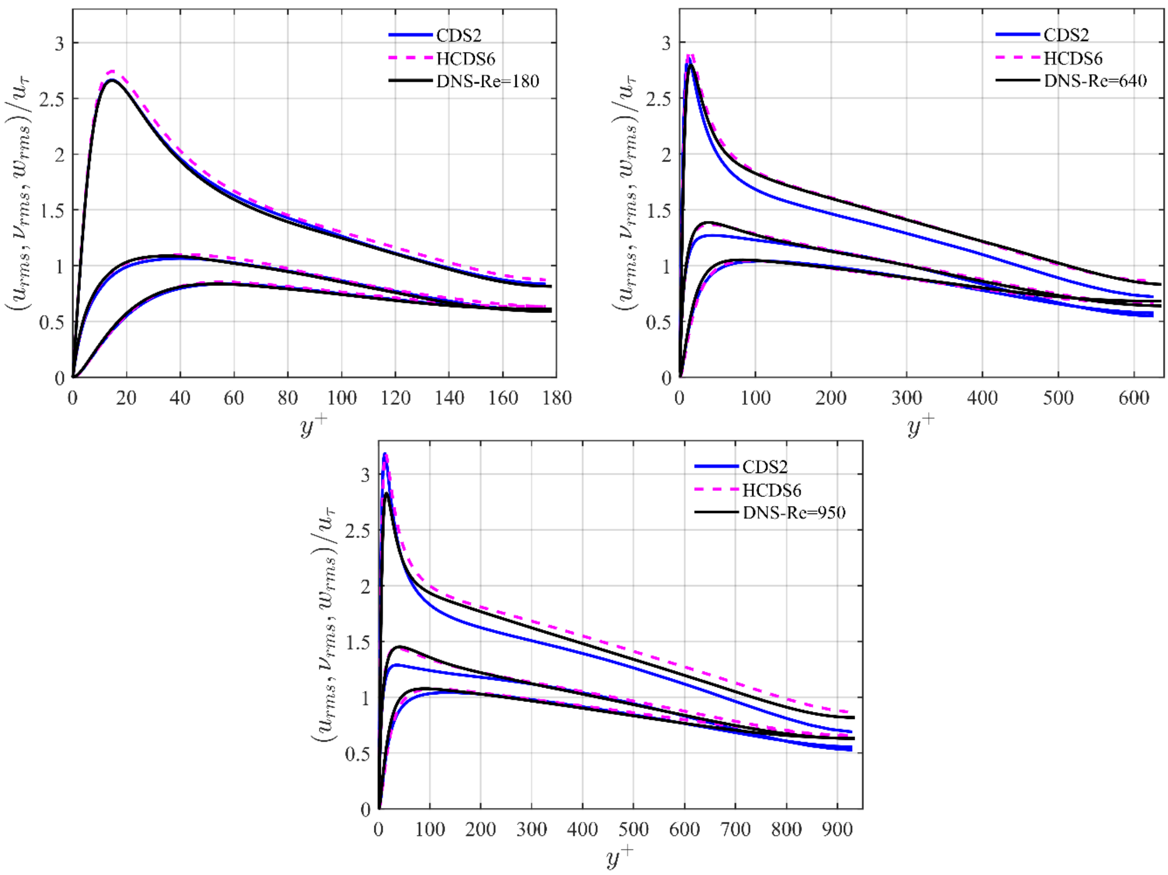

Figure 12 Velocity fluctuations in streamwise (u_{rms}), wall normal (v_{rms}) and spanwise (w_{rms}) direction as a function of the distance to the wall (y^+) for the TNS of turbulent channel flow at $Re_\tau = 180, 640, 950$

- Quantification of the under-resolution

Two dimensionless cell Reynolds numbers based on vorticity and strain term are defined to assess the resolution level of each of the TNS. The cell Reynolds Number based on vorticity ($Re_\Delta - \omega$) and strain term ($Re_\Delta - S$) is defined as:

$$Re_\Delta - \omega = \frac{\langle \omega \rangle (\sqrt[3]{\Delta x \Delta y \Delta z})^2}{\upsilon}$$
$$Re_\Delta - S = \frac{\langle S \rangle (\sqrt[3]{\Delta x \Delta y \Delta z})^2}{\upsilon} \tag{18}$$

where $\langle \omega \rangle$ represents the vorticity magnitude and $\langle S \rangle$ denotes the strain rate magnitude averaged along homogeneous directions. $\sqrt[3]{\Delta x \Delta y \Delta z}$ is the characteristic cell size based on the cell volume. Δx, Δy and Δz are the cell dimensions in x, y and z directions, respectively.

Profiles of mean cell Reynolds numbers across the channel height are shown in Figure *12*. They reach a maximum value in the laminar sublayer and then decrease to a relatively flat profile towards the center of the channel. As expected, the cell Reynolds numbers increase with the Re_τ.

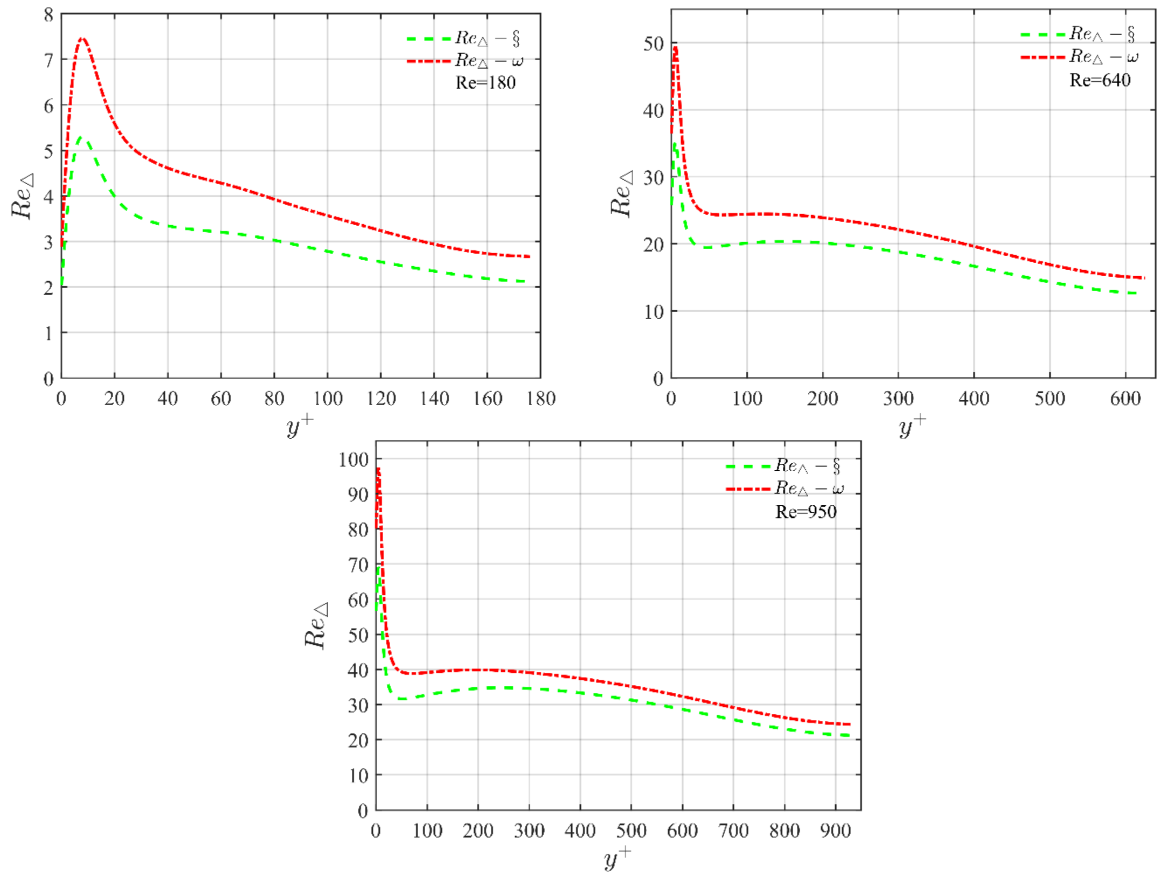

Figure 13 Mean Cell Reynolds number based on vorticity ($Re_\Delta - \omega$) and strain term ($Re_\Delta - S$) as a function of the distance to the wall (y^+) for the TNS of turbulent channel flow at $Re_\tau = 180, 640, 950$.

CONCLUSIONS

A new second-order finite differences scheme was introduced to discretize the convective terms of the incompressible Navier–Stokes equations on an orthogonal non-uniform staggered grid. This scheme expressed in divergence form conserves the discrete mass and momentum, with limited production or dissipation of discrete kinetic energy. Compared to the standard second-order scheme of Harlow and Welsh, the new proposed scheme is more accurate. Compared to existing fourth-order kinetic energy conserving schemes, the new scheme has a numerical stencil that is more compact, which makes its implementation and the treatment of boundary conditions easier.

The scheme performance is evaluated on viscous and inviscid flow simulations conducted on both uniform and non-uniform grids. In a grid-convergence analysis applied to the advection of an isentropic vortex, the RMSE of the vortex velocity using the HCDS6 scheme is reduced by two orders of magnitude compared to the standard second-order central scheme. For the Taylor-Green vortex flow, iso-contours of the vorticity norm in the midplane close to the dissipation peak are compared with a DNS reference. Complex vortical structures are better captured by the HCDS6 than the standard second-order scheme. The under-resolved turbulent channel flow benchmark is a challenging case to investigate the stability and accuracy of the scheme on a non-uniform grid. Simulations show the HCDS6 remains stable even if the simulations are getting highly under-resolved (by increasing the friction Reynolds number). The flow statistics are comparable to the standard second-order scheme. It proves that, even though the HCDS6 does not strictly conserve the discrete kinetic energy, it does not affect the numerical stability and flow statistics.

The new scheme is an alternative to the existing central scheme for incompressible flow on staggered mesh. It should facilitate the use of staggered grids in combination with complex geometries modeled using immersed boundary methods (IBM).

APPENDIX

For an initial condition $u(x,0) = e^{ikx}$, the exact solution of the form:

$$u(x,t) = e^{ik(x-at)} \quad (19)$$

is admitted. Here k is the wavenumber.

The numerical solution can be expressed in terms of its Fourier series:

$$u_j(t) = \sum_k u_k(t) e^{ikx_j} \quad (20)$$

where u_k is the amplitude of the k^{th}Fourier mode.

The Fourier transform of the semi-discretized equation (8) is obtained by substituting $u_j(t)$ from equation (20):

$$\frac{\partial u_k(t)}{\partial t} e^{ikx_j} = -\frac{a u_k(t)}{2h}\left(\frac{1}{30}e^{3ikh} - \frac{3}{10}e^{2ikh} + \frac{3}{2}e^{ikh} - \frac{3}{2}e^{-ikh} + \frac{3}{10}e^{-2ikh} - \frac{1}{30}e^{-3ikh}\right) e^{ikx_j} \quad (21)$$

And is simplified using the Euler's formula $\left(e^{\pm ikh} = \cos kh \pm i \sin kh\right)$:

$$\frac{\partial u_k(t)}{\partial t} = -\frac{ai}{h}\left(\frac{1}{30}sin(3kh) - \frac{3}{10}sin(2kh) + \frac{3}{2}sin(kh)\right) u_k(t) \quad (22)$$

The solution of Equation (22) in Fourier space can be written as:

$$u_k(t) = e^{-\frac{ai}{h}\left(\frac{1}{30}sin\,3kh - \frac{3}{10}sin\,2kh + \frac{3}{2}sin\,kh\right)t} \quad (23)$$

Substituting this expression into Equation (20), the numerical solution can be obtained in physical space:

$$u_j(t) = \sum_k e^{i\left(kx_j - \frac{at}{h}\left(\frac{1}{30}sin(3kh) - \frac{3}{10}sin(2kh) + \frac{3}{2}sin(kh)\right)\right)} \quad (24)$$

Comparing the exact and numerical solutions of the 1D linear advection equation (Equations (19) and (24)), the non-dimensional modified wavenumber $\tilde{k}_{mod} = k_{mod}h$ reads as a function of the non-dimensional wavenumber $\xi = kh$:

$$\tilde{k}_{mod} = \frac{1}{30}sin(3\xi) - \frac{3}{10}sin(2\xi) + \frac{3}{2}sin(\xi) \quad (25)$$

The dispersion relation $(\omega = ka)$ and phase velocity (ω/k) becomes:

$$\omega = \frac{a}{h}\left(\frac{1}{30}sin(3\xi) - \frac{3}{10}sin(2\xi) + \frac{3}{2}sin(\xi)\right)$$
$$\frac{\omega}{k} = \frac{a}{\xi}\left(\frac{1}{30}sin(3\xi) - \frac{3}{10}sin(2\xi) + \frac{3}{2}sin(\xi)\right) \quad (26)$$

REFERENCES

1. Mittal, R. and G. Iaccarino, *IMMERSED BOUNDARY METHODS.* Annual Review of Fluid Mechanics, 2005. **37**(1): p. 239-261.
2. Yalla, G.R., *Numerical discretization effects in large eddy simulation of turbulence*. 2022.
3. Kravchenko, A. and P. Moin, *On the effect of numerical errors in large eddy simulations of turbulent flows.* Journal of computational physics, 1997. **131**(2): p. 310-322.
4. Ghosal, S., *An analysis of numerical errors in large-eddy simulations of turbulence.* Journal of Computational Physics, 1996. **125**(1): p. 187-206.
5. Glendening, J.W. and T. Haack, *Influence of advection differencing error upon large-eddy simulation accuracy.* Boundary-layer meteorology, 2001. **98**: p. 127-153.
6. Chow, F.K. and P. Moin, *A further study of numerical errors in large-eddy simulations.* Journal of Computational Physics, 2003. **184**(2): p. 366-380.
7. Gullbrand, J. and F.K. Chow, *The effect of numerical errors and turbulence models in large-eddy simulations of channel flow, with and without explicit filtering.* Journal of Fluid Mechanics, 2003. **495**: p. 323-341.
8. Canuto, C., et al., *Spectral methods: fundamentals in single domains*. 2007: Springer Science & Business Media.
9. Nagarajan, S., S.K. Lele, and J.H. Ferziger, *A robust high-order compact method for large eddy simulation.* Journal of Computational Physics, 2003. **191**(2): p. 392-419.
10. Laizet, S. and E. Lamballais, *High-order compact schemes for incompressible flows: A simple and efficient method with quasi-spectral accuracy.* Journal of Computational Physics, 2009. **228**(16): p. 5989-6015.
11. Armfield, S., *Finite difference solutions of the Navier-Stokes equations on staggered and non-staggered grids.* Computers & fluids, 1991. **20**(1): p. 1-17.
12. Komen, E.M.J., et al., *Analysis of the numerical dissipation rate of different Runge–Kutta and velocity interpolation methods in an unstructured collocated finite volume method in OpenFOAM®.* Computer Physics Communications, 2020. **253**: p. 107145.
13. Harlow, F.H. and J.E. Welch, *Numerical calculation of time-dependent viscous incompressible flow of fluid with free surface.* The physics of fluids, 1965. **8**(12): p. 2182-2189.
14. Ham, F., F. Lien, and A. Strong, *A fully conservative second-order finite difference scheme for incompressible flow on nonuniform grids.* Journal of Computational Physics, 2002. **177**(1): p. 117-133.
15. Moin, P. and R. Verzicco, *On the suitability of second-order accurate discretizations for turbulent flow simulations.* European Journal of Mechanics-B/Fluids, 2016. **55**: p. 242-245.
16. Orlandi, P., *A numerical method for direct simulation of turbulence in complex geometries.* Annual Research Briefs, 1989, 1990: p. 215-229.
17. Duponcheel, M., P. Orlandi, and G. Winckelmans, *Time-reversibility of the Euler equations as a benchmark for energy conserving schemes.* Journal of Computational Physics, 2008. **227**(19): p. 8736-8752.
18. Kálnay de Rivas, E., *On the use of nonuniform grids in finite-difference equations.* Journal of Computational Physics, 1972. **10**(2): p. 202-210.
19. Tian, Z., X. Liang, and P. Yu, *A higher order compact finite difference algorithm for solving the incompressible Navier–Stokes equations.* International Journal for Numerical Methods in Engineering, 2011. **88**(6): p. 511-532.
20. Morinishi, Y., *Conservative properties of finite difference schemes for incompressible flow.* Center for Turbulence Research Annual Research Briefs: 1995, 1995.
21. Morinishi, Y., et al., *Fully conservative higher order finite difference schemes for incompressible flow.* Journal of computational physics, 1998. **143**(1): p. 90-124.
22. Vasilyev, O.V., *High order finite difference schemes on non-uniform meshes with good conservation properties.* Journal of Computational Physics, 2000. **157**(2): p. 746-761.
23. Verstappen, R. and A. Veldman, *Direct numerical simulation of turbulence at lower costs.* Journal of Engineering Mathematics, 1997. **32**: p. 143-159.

24. Verstappen, R. and A. Veldman, *Symmetry-preserving discretization of turbulent flow.* Journal of Computational Physics, 2003. **187**(1): p. 343-368.
25. Bihs, H., et al., *A new level set numerical wave tank with improved density interpolation for complex wave hydrodynamics.* Computers & Fluids, 2016. **140**: p. 191-208.
26. Berthelsen, P.A. and O.M. Faltinsen, *A local directional ghost cell approach for incompressible viscous flow problems with irregular boundaries.* Journal of computational physics, 2008. **227**(9): p. 4354-4397.
27. Tseng, Y.-H. and J.H. Ferziger, *A ghost-cell immersed boundary method for flow in complex geometry.* Journal of computational physics, 2003. **192**(2): p. 593-623.
28. Chorin, A.J., *Numerical solution of the Navier-Stokes equations.* Mathematics of computation, 1968. **22**(104): p. 745-762.
29. Van der Vorst, H.A., *Bi-CGSTAB: A fast and smoothly converging variant of Bi-CG for the solution of nonsymmetric linear systems.* SIAM Journal on scientific and Statistical Computing, 1992. **13**(2): p. 631-644.
30. Falgout, R.D., J.E. Jones, and U.M. Yang, *Conceptual interfaces in hypre.* Future Generation Computer Systems, 2006. **22**(1-2): p. 239-251.
31. Shu, C.-W. and S. Osher, *Efficient implementation of essentially non-oscillatory shock-capturing schemes.* Journal of computational physics, 1988. **77**(2): p. 439-471.
32. Weinan, E. and J.-G. Liu, *Projection method I: convergence and numerical boundary layers.* SIAM journal on numerical analysis, 1995: p. 1017-1057.
33. Bricteux, L., S. Zeoli, and N. Bourgeois, *Validation and scalability of an open source parallel flow solver.* Concurrency and Computation: Practice and Experience, 2017. **29**(21): p. e4330.
34. Kim, J., P. Moin, and R. Moser, *Turbulence statistics in fully developed channel flow at low Reynolds number.* Journal of fluid mechanics, 1987. **177**: p. 133-166.
35. Moser, R.D., J. Kim, and N.N. Mansour, *Direct numerical simulation of turbulent channel flow up to Re τ= 590.* Physics of fluids, 1999. **11**(4): p. 943-945.